ELSEVIER

00 February 2002

Optics Communications xxx (2002) xxx–xxx

OPTICS COMMUNICATIONS

www.elsevier.com/locate/optcom

The case of a spherical wave front for the generalized Lorenz–Mie theory including a comparison to experimental data

J. Ascención Guerrero [a], F. Mendoza Santoyo [a,*], D. Moreno [a], M. Funes-Gallanzi [b]

[a] *Centro de Investigaciones en Optica, Loma del Bosque 115, Colonia Lomas del Campestre, León, Guanajuato, Mexico*
[b] *Instituto Nacional de Astrofísica, Optica y Electrónica (INAOE), Luis Enrique Erro 1, Tonantzintla, Puebla, Mexico*

Received 14 June 2001; accepted 28 January 2002

Abstract

Scattering light from a spherical particle located on-axis to an electromagnetic spherical wave is numerically predicted using the generalized Lorenz–Mie theory (GLMT). The model is compared to the classical Lorenz–Mie theory, plane wave case, and to experimental in-line Fraunhofer holograms of spherical particles, showing good agreement. Fundamental questions germane to velocimetry applications and seeding particle positioning are discussed. © 2002 Published by Elsevier Science B.V.

PACS: 42.68.M; 42.25.F; 42.40kw

1. Introduction

The scattering of an electromagnetic wave by a dielectric sphere has been thoroughly investigated for more than a century and there is a huge body of literature about the subject. The scattering by such a sphere is referred to as Mie theory, although Mie [1] was not the first to formulate this electromagnetic scattering problem. Before him Alfred Clebsh (1833–72) and Ludvig Lorenz (1829–91) contributed to this problem. The first modern outline of the Mie theory in terms of a spherical vector wave-function is given in the classical book by Stratton [2]. Mie theory is a variables separation approach which gives an analytical equation for the Mie coefficients. Mie theory is restricted to plane wave scattering by a spherical homogeneous, isotropic and non-magnetic particle in a non-absorbing medium.

More advanced theoretical and experimental techniques depend on the ability to handle a more general problem where the scatter center is illuminated by a laser beam, having led to the so-called generalized Lorenz–Mie theory (GLMT).

* Corresponding author. Tel.: +52-4773-1017; fax: +52-4717-5000.
E-mail addresses: fmendoza@foton.cio.mx (F. Mendoza Santoyo), dmh@andromeda.cio.mx (D. Moreno), gallanzi@inaoep.mx (M. Funes-Gallanzi).

0030-4018/02/$ - see front matter © 2002 Published by Elsevier Science B.V.
PII: S0030-4018(02)01168-9

The GLMT is a generalization of the Lorenz–Mie Theory for arbitrary incident shaped beams [3] that can also be applied, for instance, to particle-sizing. Gaussian beam techniques have been extensively explored and applied in the analysis and improvement of practical devices such as phase Doppler systems. Recently, these techniques have been applied to three-dimensional position estimation of seeding particles in velocimetry by directly analyzing the scattering pattern with real-time CCD cameras [4,5]. In this case, particle scattering need to be calculated and then propagated through an aperture and lens system to an image plane for comparison to experimentally derived images and thus derive particle position.

Recently, a new technique was developed called tunneling velocimetry (TV) for three-dimensional fluid flow measurement [6], which is an improvement on the well-known technique of particle image velocimetry (PIV). In the TV technique, the flow is seeded with particles such as polystyrene spheres. A collimated laser beam is introduced into the optical axis of a video detector by a polarizing beam-splitter arrangement and thus illuminates the flow field. The polarizing beam-splitter also transmits the scattered light onto the imaging lens and CCD camera. The laser is pulsed and the CCD camera records multiple images of the light scattered by the seeding particles. If we want a high interrogation area, it is necessary to expand the illumination source into a spherical wave. Moreover, in the case of holographic PIV the volume of interest is often illuminated by a spherical wave front, and it is therefore of interest to be able to estimate particle position from these holographic recordings. Thus, the need to further develop the GLMT for the case of light scattered by spherical particles illuminated with a spherical wave front. A spherical wave front makes particle positioning more exact because digital image representation changes makes it approximately 30 times more sensitive to a depth movement than the same particle illuminated by a plane wave front [7].

2. The GLMT for a electromagnetic spherical wave

The GLMT is a generalization of Lorenz–Mie theory for arbitrary incident shaped beams such as Gaussian, light sheet and top hat beams. GLMT describes the angular and integral properties (amplitudes, intensities, phase angle, cross-section including radiation pressure cross-section) of the light scattered by an ideal sphere arbitrarily located in an arbitrary shaped beam. Formalism details can be found in [8].

The geometry used for the incident field and particle location is defined in Fig. 1. Consider two Cartesian co-ordinate systems ($O_{PS}uvw$) and ($O_p xyz$), attached to the incident field and to the particle center, respectively, with $O_{PS}u$ parallel to $O_p x$ and $O_{PS}v$ parallel to $O_p y$. O_{PS} and O_p are the point source localization for a spherical wave and the particle center, respectively. The incident field is linearly polarized, propagating towards the positive w-axis with the electric field **E** parallel to

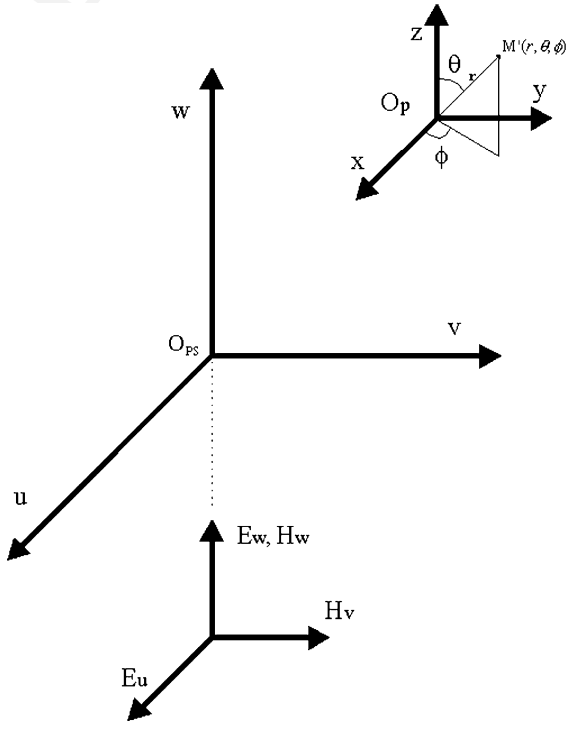

Fig. 1. System geometry for the GLMT calculations using a spherical wave front.

the u-axis. The scattered light is observed at point $M'(r,\theta,\varphi)$, where r, θ, φ are spherical co-ordinates attached to the particle system $(O_{\mathrm{p}}xyz)$.

2.1. Incident field description

In this section we derive the vectorial form of the incident field, for a vectorial spherical wave. The expressions for this wave assume its most convenient form with the Hertz vector, which represents the radiation emitted by a linearly oscillating dipole. The magnetic field lines are circles about the direction of oscillation, while the electric field lines are the meridian planes of that direction.

A physical light source contains all possible directions of oscillation. Such a source emits an average field in which no single direction is preferred. The field intensity is therefore spherically symmetric. Furthermore, a field intensity emanating from an ideal lens or a pinhole is spherically symmetric too. Thus, we may model the electromagnetic spherical wave as it emanates from a point source of unit strength.

In the TM-mode, the electric field E is polarized parallel to the u-axis, i.e. $E_v = E_w = 0$ and consequently $H_u = 0$. We consider a point source of unit strength located at the position (u_0, v_0, w_0). Thus, the field equation in the presence of a source satisfies the inhomogeneous wave equation [9]:

$$\left(\frac{\partial^2}{\partial u^2}+\frac{\partial^2}{\partial v^2}+\frac{\partial^2}{\partial w^2}+k^2\right)E_u = \delta(u-u_0)\delta(v-v_0)\delta(w-w_0), \tag{1}$$

where $k=\omega_0(\varepsilon_0\mu_0)^{1/2}=2\pi/\lambda$, λ is the point source light wavelength and ω is the angular frequency. In the TE-mode, the magnetic field H is polarized parallel to the u-axis, i.e. $H_v = H_w = E_u = 0$ and H_u satisfies Eq. (1).

Eq. (1) can be solved by using Green's functions. Green's function that satisfies the inhomogeneous wave equation is given as

$$G(r_1,r_2)=\frac{\mathrm{e}^{\mathrm{i}k|r_1-r_2|}}{4\pi|r_1-r_2|}, \tag{2}$$

where r_1 and r_2 are position vectors representing the field point and source point, respectively. Thus, the electric field can be obtained from Green's function expressions given by Eq. (2), as

$$E_u=\frac{\mathrm{e}^{\mathrm{i}k|r_1-r_2|}}{4\pi|r_1-r_2|}. \tag{3}$$

Eq. (3) represents the electric field of a diverging spherical wave from a point source. From Eq. (3), we obtain by simple projections the field components in the (r,θ,ϕ) system:

$$E_r=\cos\phi\sin\theta\frac{\mathrm{e}^{(\mathrm{i}k|r_1-r_2|)}}{4\pi|r_1-r_2|}, \tag{4}$$

$$E_\theta=\cos\phi\cos\theta\frac{\mathrm{e}^{(\mathrm{i}k|r_1-r_2|)}}{4\pi|r_1-r_2|}, \tag{5}$$

$$E_\phi=\sin\phi\frac{\mathrm{e}^{(\mathrm{i}k|r_1-r_2|)}}{4\pi|r_1-r_2|}. \tag{6}$$

In a similar way the magnetic components can be determined

$$H_r=\sin\phi\sin\theta\frac{\mathrm{e}^{(\mathrm{i}k|r_1-r_2|)}}{4\pi|r_1-r_2|}, \tag{7}$$

$$H_\theta=\sin\phi\cos\theta\frac{\mathrm{e}^{(\mathrm{i}k|r_1-r_2|)}}{4\pi|r_1-r_2|}, \tag{8}$$

$$H_\phi=-\cos\phi\frac{\mathrm{e}^{(\mathrm{i}k|r_1-r_2|)}}{4\pi|r_1-r_2|}. \tag{9}$$

The radial components E_r and H_{r} play a special role in the theory because we need to know them to derive the beam shape coefficients (BSCs).

2.2. Scattered near field components

According to [8] the scattering field components in the near field are described as

$$\tilde{E}_r^{(s)}=-kE_0\sum_{n=1}^{\infty}\sum_{m=-n}^{+n}C_n^{\mathrm{PW}}a_n g_{n,\mathrm{TM}}^m \times\left[\xi_n(\alpha\tilde{r})+\xi_n''(\alpha\tilde{r})\right]P_n^{|m|}(\cos\theta)\mathrm{e}^{(\mathrm{i}m\phi)}, \tag{10}$$

$$\tilde{E}_{\theta}^{(s)} = -\frac{E_0}{\tilde{r}} \sum_{n=1}^{\infty} \sum_{m=-n}^{+n} C_n^{\mathrm{PW}} \times \left[a_n g_{n,\mathrm{TM}}^m \xi_n'(\alpha\tilde{r}) \tau_n^{|m|}(\cos\theta) + m b_n g_{n,\mathrm{TE}}^m \xi_n(\alpha\tilde{r}) \Pi_n^{|m|}(\cos\theta) \right] \mathrm{e}^{(\mathrm{i}m\phi)}, \quad (11)$$

$$\tilde{E}_{\phi}^{(s)} = -\frac{\mathrm{i}E_0}{\tilde{r}} \sum_{n=1}^{\infty} \sum_{m=-n}^{+n} C_n^{\mathrm{PW}} \times \left[m a_n g_{n,\mathrm{TM}}^m \xi_n'(\alpha\tilde{r}) \Pi_n^{|m|}(\cos\theta) + b_n g_{n,\mathrm{TE}}^m \xi_n(\alpha\tilde{r}) \tau_n^{|m|}(\cos\theta) \right] \mathrm{e}^{(\mathrm{i}m\phi)}. \quad (12)$$

$$\tilde{H}_{r}^{(s)} = -kH_0 \sum_{n=1}^{\infty} \sum_{m=-n}^{+n} C_n^{\mathrm{PW}} a_n g_{n,\mathrm{TE}}^m \times \left[\xi_n(\alpha\tilde{r}) + \xi_n''(\alpha\tilde{r}) \right] P_n^{|m|}(\cos\theta) \mathrm{e}^{(\mathrm{i}m\phi)}, \quad (13)$$

$$\tilde{H}_{\theta}^{(s)} = \frac{H_0}{\tilde{r}} \sum_{n=1}^{\infty} \sum_{m=-n}^{+n} C_n^{\mathrm{PW}} \times \left[m a_n g_{n,\mathrm{TM}}^m \xi_n(\alpha\tilde{r}) \Pi_n^{|m|}(\cos\theta) - b_n g_{n,\mathrm{TE}}^m \xi_n'(\alpha\tilde{r}) \tau_n^{|m|}(\cos\theta) \right] \mathrm{e}^{(\mathrm{i}m\phi)}, \quad (14)$$

$$\tilde{H}_{\phi}^{(s)} = \frac{\mathrm{i}H_0}{\tilde{r}} \sum_{n=1}^{\infty} \sum_{m=-n}^{+n} C_n^{\mathrm{PW}} \times \left[a_n g_{n,\mathrm{TM}}^m \xi_n(\alpha\tilde{r}) \tau_n^{|m|}(\cos\theta) - m b_n g_{n,\mathrm{TE}}^m \xi_n'(\alpha\tilde{r}) \Pi_n^{|m|}(\cos\theta) \right] \mathrm{e}^{(\mathrm{i}m\phi)}, \quad (15)$$

where

$$\alpha = ka \quad (16)$$

is the size parameter, k is the wave number of the incident beam, a is the particle radius, a_n and b_n are the partial-wave scattering amplitudes of plane-wave Mie theory, ψ_n, χ_n, and $\xi_n = \psi_n - \mathrm{i}\chi_n$ are the Riccati–Bessel functions, which are related to the Bessel functions of half-integer order; $P_n^{|m|}(\cos\theta)$ are the associated Legendre polynomials, depending uniquely on the observation direction. $\bar{n}$ is the complex refractive index of the sphere, and $\tilde{r} = r/a$ is the normalized distance from the particle to the scattered light observation point M'. All variables having the symbol $\sim$ are normalized with respect to the particle radius. Primed quantities denote differentiation with respect to the argument of the function. The beam shape coefficients, $g_{n,\mathrm{TM,TE}}^m$, are specific to GLMT and involve the characterization of the incident beam. They are described by use of expansions into partial waves expressed in the spherical coordinate system (r, θ, ϕ), and can be determined from the mathematical expressions of the radial electric field E_r (for $g_{n,\mathrm{TM}}^m$) and the radial magnetic field H_r (for $g_{n,\mathrm{TE}}^m$), by use of the quadrature, the finite series method or localized approximations.

2.3. The BSC computations

Different methods have been developed to compute the BSCs. A rigorous approach is based on the surface integral [10]. The coefficients of a Gaussian beam can also be computed by finite series for on-axis particle positions [11]. The localized approximation of the beam shape coefficients leads to the fastest algorithm, as has been demonstrated by Lock [12]. In this paper we used a combination of the localized approximation and integral quadrature given in [13].

To ease the procedure outlined in [13], the absolute value

$$|r_1 - r_2| = \sqrt{(x - x_0) + (y - y_0) + (z - z_0)}$$

in Eqs. (4) and (7) is approximated by taking the first two terms of the binomial expansion

$$|r_1 - r_2| = z\left[1 + \frac{1}{2}\left(\frac{x - x_0}{2}\right)^2 + \frac{1}{2}\left(\frac{y - y_0}{2}\right)^2\right], \quad (17)$$

which can be transformed into spherical co-ordinates, as

$$|r_1 - r_2| = \left[(r\cos\theta - z_0) + \left\{\left[(r\sin\theta)^2 - 2r\sin\theta(x_0\cos\phi + y_0\sin\phi) + (x_0^2 + y_0^2)\right] \Big/ [2(r\cos\theta - z_0)]\right\}\right]. \quad (18)$$

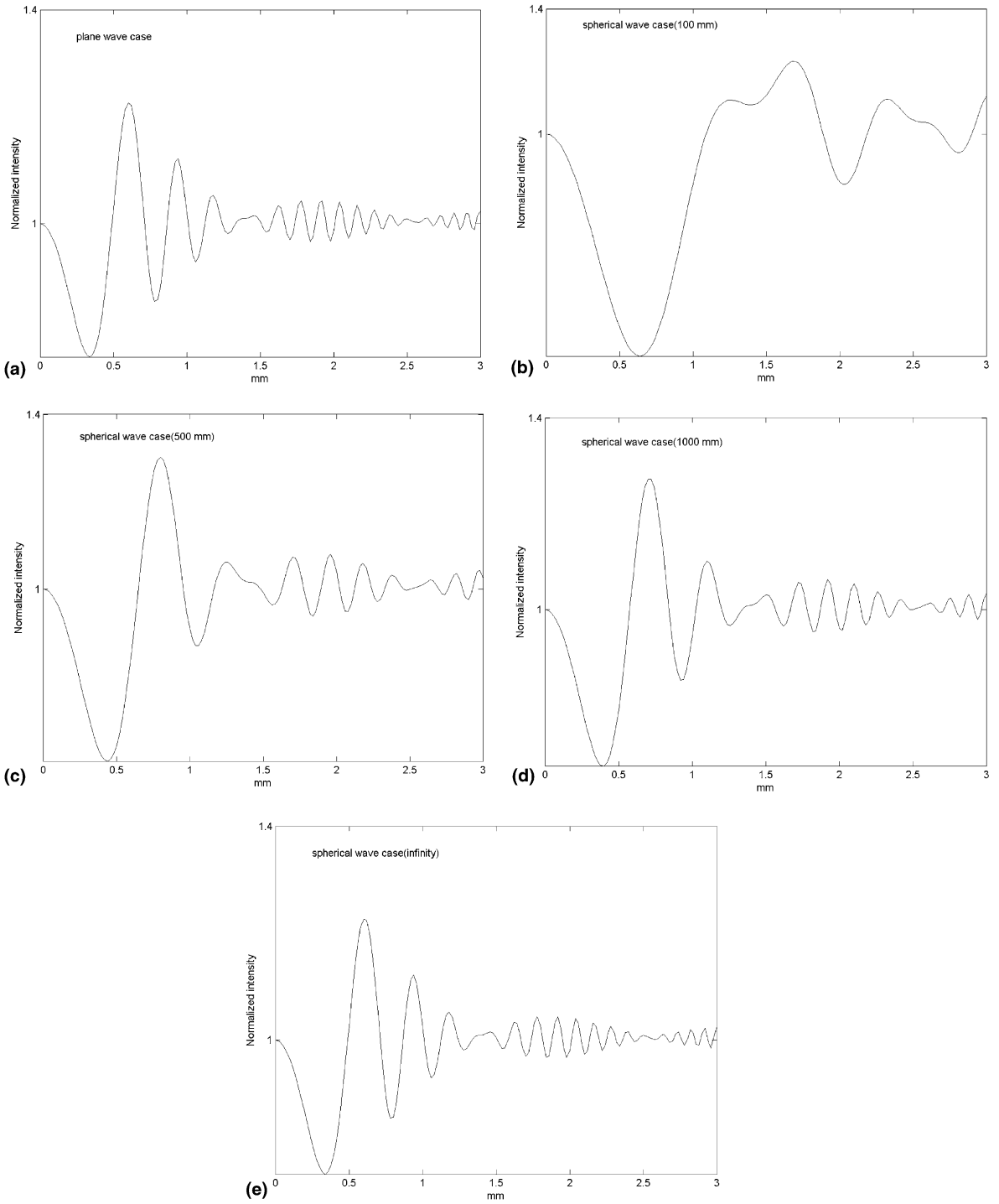

Fig. 2. Plane wave and spherical wave case comparison: (a) plane wave, (b) 0.1, (c) 0.5, (d) 1.0 and (e) 10.0 m of distance from the particle to the illumination source. The horizontal axes represents the $O_p y$ particle axis, while the vertical axes represent normalized intensity values.

Eq. (18) is substituted in Eqs. (4) and (7). For space shortness only the radial electric field is shown

$$E_r = \cos\phi \sin\theta \Bigg/ \Bigg[(r\cos\theta - z_0) + \frac{(r\sin\theta)^2 - 2r\sin\theta(x_0\cos\phi + y_0\sin\phi) + (x_0^2 + y_0^2)}{2(r\cos\theta - z_0)} \Bigg] \times \exp\Big(\mathrm{i}k \Big[(r\cos\theta - z_0) + \Big\{ \Big[(r\sin\theta)^2 - 2r\sin\theta(x_0\cos\phi + y_0\sin\phi) + (x_0^2 + y_0^2) \Big] / [2(r\cos\theta - z_0)] \Big\} \Big] \Big). \quad (19)$$

Consider the simplest case where the particle is located on-axis, thus the radial electric field is reduced to

$$E_r = \frac{\cos\phi\sin\theta}{\left[(r\cos\theta - z_0) + \frac{(r\sin\theta)^2}{2(r\cos\theta - z_0)} \right]} \times \exp\left(\mathrm{i}k \left[(r\cos\theta - z_0) + \frac{(r\sin\theta)^2}{2(r\cos\theta - z_0)} \right] \right). \quad (20)$$

The BSCs for a particle located on-axis are given as, viz. [13]

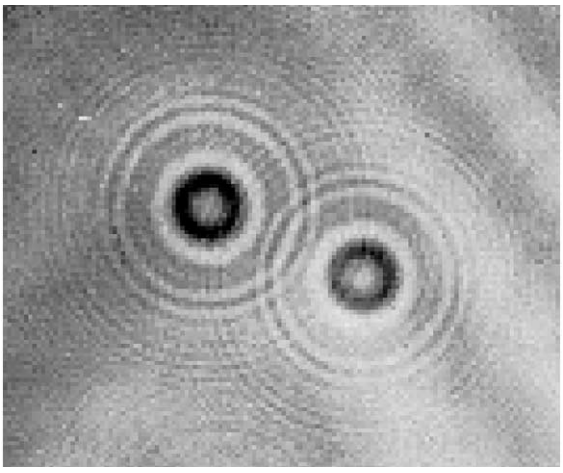

Fig. 3. Holographic image: $a = 110$ μm; $\lambda = 0.6328$; $z_1 = 40$ cm; $z_0 = 20$ cm; with a z-axis displacement of $\Delta z = 1$ cm.

$$g_{n,\mathrm{TM}}^{\pm 1} = \frac{1}{2\pi E_0} \int_0^{2\pi} \hat{G}[E_r(r,\theta,\phi)] \exp(-\mathrm{i}(\pm 1)\phi)\, \mathrm{d}\phi, \quad (21)$$

$$g_{n,\mathrm{TE}}^{\pm 1} = \frac{1}{2\pi H_0} \int_0^{2\pi} \hat{G}[H_r(r,\theta,\phi)] \exp(-\mathrm{i}(\pm 1)\phi)\, \mathrm{d}\phi. \quad (22)$$

Applying the procedure outlined in [13], we obtain the following expressions for the BSCs

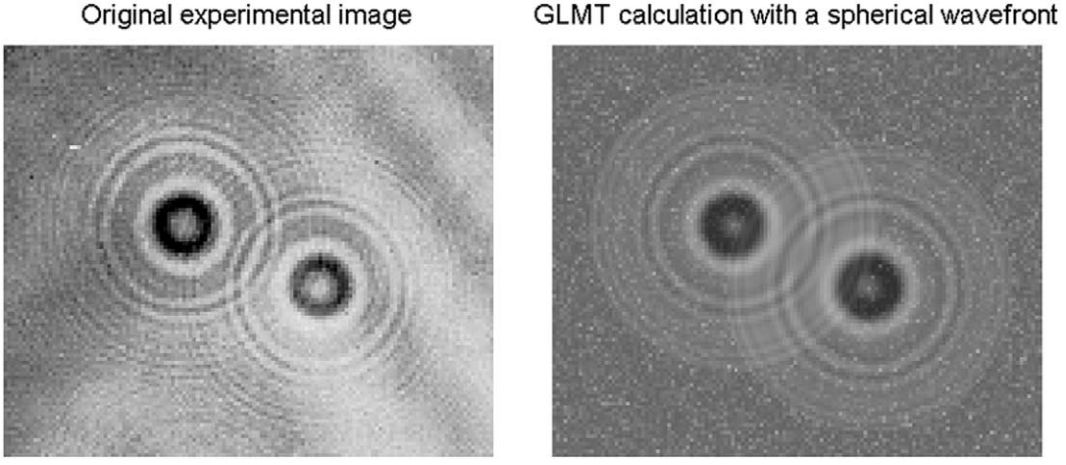

Fig. 4. Particle image scattering computed using the GLMT with a spherical wave front. The same conditions as those for the experimental data were used, particles separated by 1 cm.

$$g^{1}_{n,\mathrm{TM}} = g^{-1}_{n,\mathrm{TM}} = \frac{A}{2E_0}, \tag{23}$$

$$g^{1}_{n,\mathrm{TE}} = -g^{-1}_{n,\mathrm{TE}} = -\frac{\mathrm{i}A}{2E_0}, \tag{24}$$

where A is given as

$$A = \frac{-1}{z_0 + \frac{R^2}{2z_0}} \exp(-\mathrm{i}kz_0) \exp\left(-\mathrm{i}kR^2/2z_0\right), \tag{25}$$

where R is the rescaled co-ordinate expressed as

$$R = kr = n + 1/2. \tag{26}$$

3. Numerical and experimental results

The GLMT for the case of an electromagnetic spherical wave will be compared with the classical Lorenz–Mie theory that is, the plane wave case. Close to the source we have a spherical electromagnetic wave, but as the light source moves away from the particle the electromagnetic wave can be considered as plane. We will use this fact to compare our proposed model.

The technique used to compute the Ricatti–Bessel functions, and the coefficients a_n, b_n are described elsewhere [14]. Computation of the associated Legendre function is accomplished by using standard recursion formulas such as those presented by Abramowitz and Stegun [15]. All electric field quantities are normalized based on an assumed uniform incident electric field of unit amplitude.

The observation point M' receives light from the scattered and incident waves. The total field in the forward scatter case is composed by the incident plus scattered fields. The intensity value at the observation point M' is given by Poynting vector, as is the direction of propagation, and is symmetrical to the axis $O_{\mathrm{p}}z$. Hence, the intensity value needs only to be calculated for one axis, like O_{p}y. Fig. 2 shows forward scatter plots of a 220 μm glass spherical particle illuminated with a He–Ne laser, as the illumination source was moved away from the particle to 0.1, 0.5, 1.0, 3.0 and 10.0 m, considered for practical purposes as infinity. The vertical axes in these plots show the scattering calculations for the electromagnetic spherical wave case normalized to the central value of the intensity found at the start of the $O_{\mathrm{p}}y$-axis, shown as the horizontal axes in the plots. The plots show that the particle scattering when using a spherical wave front approximates, in the limit of a large distance, to the plane wave scattering case.

The model is also compared to experimental Fraunhofer in-line holograms of spherical particles [7]. The experiment used coherent light from a laser passed through a condensing lens-pinhole system to produce a diverging beam, which illuminated spherical particles introduced into its

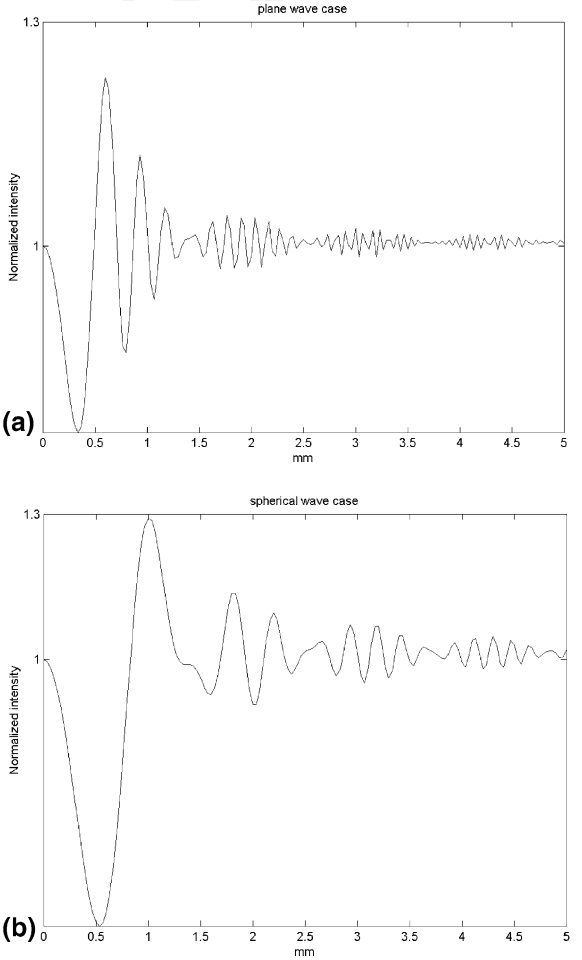

Fig. 5. Plane wave and spherical wave case comparison for the same conditions as in the experimental data. Vertical and horizontal axes as in Fig. 2.

path, at a distance z_0 from the pinhole. Light diffracted by the particles adds coherently with light that has not been diffracted, i.e. background light. The resulting amplitude distribution forms an interference pattern whose fringes are recorded as intensities on film, at a distance z_1 from the particle. The interference pattern is symmetrical about the z-axis which is the optical axis originating at the pinhole. An example of such experiment is given in Fig. 3 for two spherical particles of diameter 220 μm, separated 1 cm from each other. Fig. 4 shows the results from the theoretical model when using the same conditions than those for the experimental result, where some background fringes are seen to dark some places on the experimental image. These fringes are due to experimental conditions typical of a holographic experiment, and are not simulated in the theoretical model, hence the theoretical model and experimental data show good agreement. Fig. 5 shows the convenience of using the GLMT with an electromagnetic spherical wave, depicting the difference with the plane wave case for the same experimental conditions.

4. Conclusions

For the first time, the formulation of a spherical wave front in the context of the generalized Lorenz–Mie theory is presented. This is important for velocimetry applications for two reasons:

(a) a larger region of interest can be illuminated,
(b) the positioning of seeding particles is more accurate, as the digital representation of the particle image now changes, not only due to particle and lens characteristics, but also due to the changing incident field for varying positions.

Theoretical results have been compared to experimental results and found to be in good agreement.

Much work remains to be done in the area of high-accuracy three-dimensional position estimation of seeding particles in velocimetry applications. Current research is focussed on producing an optical system capable of expanding a collimated beam into a spherical wave front for illumination purposes and to act as a lens relay for the scattered light. With the aid of advances such as those discussed in this work, the capabilities of velocimetry are being extended to yield high-accuracy volumetric particle positioning and thereby improve volumetric velocity estimates, used to address many fundamental questions in fluid dynamics research.

References

[1] G. Mie, Ann. Phys. 25 (1908) 377.
[2] J.A. Stratton, Electromagnetic Theory, McGraw-Hill, New York, 1941.
[3] G. Gouesbet, G. Grehan, B. Maheu, J. Opt. 16 (1985) 83.
[4] D. Moreno, F. Mendoza, J. Guerrero, M.F. Gallanzi, Appl. Opt. 39 (2000) 5117.
[5] J.A. Guerrero, F. Mendoza, D. Moreno, M. Funes-Gallanzi, Meas. Sci. Tech. 11 (2000) 568.
[6] M.F. Gallanzi, in: R.J. Adrian (Ed.), Proceedings of the 10th International Laser Anemometry in Fluids Mechanics, vol. X, Technico Institute, Lisbon, 2000.
[7] R. Menzel, F.M. Shofener, Appl. Opt. 9 (1970) 2073.
[8] G. Gousbet, B. Maheu, G. Gréhan, J. Opt. Soc. Am. A 5 (1994) 165.
[9] J.D. Jackson, in: Classical Electrodynamical, Wiley, New York, 1975, p. 183.
[10] G. Gouesbet, C. Letellier, K.F. Ren, G. Gréhan, Appl. Opt. 35 (1996) 1537.
[11] G. Gouesbet, G. Gréhan, B. Maheu, J. Opt. 19 (1998) 35.
[12] G. Gréhan, B. Maheu, G. Gouesbet, Appl. Opt. 25 (1986) 3539.
[13] K.F. Ren, G. Gouesbet, G. Grehan, Appl. Opt. 37 (1998) 4218.
[14] J.V. Dave, IBM J. Res. Dev. 13 (1969) 302.
[15] M. Abramowitz, I.A. Stegun, in: Handbook of Mathematical Functions, Dover, New York, 1972, pp. 332–334.